

# Overcoming Zinc Oxide Interface Instability with a Methylammonium-free Perovskite for High Performance Solar Cells

Kelly Schutt,<sup>1</sup> Pabitra K. Nayak,<sup>1</sup> Alexandra J. Ramadan,<sup>1</sup> Bernard Wenger,<sup>1</sup> Yen-Hung Lin,<sup>1</sup> Henry J. Snaith\*<sup>1</sup>

<sup>1</sup> Clarendon Laboratory, Department of Physics, University of Oxford, Parks Road, Oxford OX1 3PU, United Kingdom

## Abstract

Perovskite solar cells have achieved the highest power conversion efficiencies on metal oxide n-type layers, including SnO<sub>2</sub> and TiO<sub>2</sub>. Despite ZnO having superior optoelectronic properties to these metal oxides, such as improved transmittance, higher conductivity, and closer conduction band alignment to methylammonium (MA)PbI<sub>3</sub>, ZnO has largely been overlooked due to a chemical instability when in contact with metal halide perovskites, which leads to the rapid decomposition of the perovskite. While surface passivation techniques have somewhat mitigated this instability, investigations as to whether all metal halide perovskites exhibit this instability with ZnO are yet to be undertaken. We develop experimental methods to elucidate the degradation mechanisms at ZnO-MAPbI<sub>3</sub> interfaces. By substituting MA with formamidinium (FA) and cesium (Cs), we greatly enhance the stability of the perovskite-ZnO interface and find that stability compares favorably with SnO<sub>2</sub>-based devices after high intensity UV irradiation and 85 °C thermal stressing. For devices comprising FA and Cs based metal halide perovskite absorber layers on ZnO, we achieve 21.1% scanned power conversion efficiency and 18% steady-state power output. Our work demonstrates that ZnO appears to be as feasible an n-type charge extraction layer as SnO<sub>2</sub>, with many foreseeable advantages, provided that we move away from MA cations.

## Introduction

Organic-inorganic metal halide perovskites are promising next generation materials for solar cells due to their tunable band gap, long carrier diffusion length, strong optical absorption, defect tolerance, use of low cost materials, and high power conversion efficiency (PCE).<sup>[1–4]</sup> To date, perovskite solar cells (PSC) with record PCE have been lead by devices with metal oxide n-type layers, with PCE now reaching 23.7%.<sup>[5]</sup> Despite impressive gains in PCE, often material choices made to deliver the highest efficiencies neglect the essential requirement for simultaneously delivering high stability. Understanding the unique degradation mechanisms present at metal oxide-perovskite interfaces is especially vital, and degradation kinetics between different metal oxides and perovskites vary dramatically. TiO<sub>2</sub>-perovskite interfaces are notably unstable under UV light,<sup>[6]</sup> and a recent test of 1,000 hour operational performance showed devices utilizing SnO<sub>2</sub> achieved longer lifetimes than those with TiO<sub>2</sub>.<sup>[7]</sup> SnO<sub>2</sub>-perovskite interfaces, which we show here to offer greatly improved UV stability relative to TiO<sub>2</sub>, also introduce a thermal instability, that is just now being addressed through surface passivation.<sup>[8]</sup>

While TiO<sub>2</sub> and SnO<sub>2</sub> have been favored candidates for n-type charge extraction layers, ZnO has received comparatively little attention due to a greatly reduced thermal stability and, historically, lower performance.<sup>[9,10]</sup> However, the opto-electronic properties of ZnO are encouraging: relative to polycrystalline TiO<sub>2</sub> and SnO<sub>2</sub>, ZnO offers greater transmittance in the visible to IR regions of the spectrum and lower resistivity,<sup>[11]</sup> orders of magnitude higher mobility resulting in part from a lower effective electron mass,<sup>[12,13]</sup> and a shallower conduction band edge that may align more closely with metal halide perovskites.<sup>[14]</sup> This suggests that if stability issues are overcome, ZnO could deliver improved fill factor from higher conductivity and increased voltages due to improved energetic alignment at the perovskite interface. Additionally, ZnO crystallizes at lower

temperature, and hence offers lower energy processing routes than solution processed  $\text{TiO}_2$  or  $\text{SnO}_2$ , with colloidal nanoparticle synthesis techniques enabling low temperature annealing or even room temperature deposition, making it suitable for flexible polymer substrates.<sup>[15,16]</sup>

Furthermore, aluminum doped ZnO (AZO) is also a very useful transparent conducting oxide (TCO) which avoids the resource scarcity of indium, in indium tin oxide (ITO), making it more suitable for use as an electrode in PSC at TW scale production. A recent life-cycle assessment of perovskite-on-silicon tandem modules has revealed that Indium in the TCO accounts for 29% of the total ecotoxicological environmental impact.<sup>[17]</sup> In addition, for TCO's on flexible willow glass it was found that AZO offers improved transmittance and lower sheet resistance in comparison to ITO (85.8% to 81.5% and 17.8  $\Omega/\text{sq}$  to 31.3  $\Omega/\text{sq}$ , respectively).<sup>[18]</sup> Therefore, interfacing AZO with ZnO would appear to be a very useful combination of TCO and n-type charge extraction layer.

The ZnO-perovskite interface instability has been widely reported, with a variety of degradation mechanisms proposed. Cheng et. al. experimentally demonstrated that hydroxyl groups present on zinc oxide nanoparticles accelerate  $\text{MAPbX}_3$  degradation; higher temperature annealing of ZnO decreased the surface density of hydroxyl groups and improved perovskite stability. However, the perovskite films still turned yellow after 30 minutes of annealing at 100 °C.<sup>[19]</sup> Dkhissi et. al. reported slightly greater release of physisorbed water from ZnO than from  $\text{TiO}_2$  at temperatures above 70 °C, but found this incapable of explaining the stability variation between the two metal oxides. They proposed that as  $\text{CH}_3\text{NH}_3\text{I}$  decomposes into  $\text{CH}_3\text{NH}_2 + \text{HI}$ , the HI could react with ZnO to form  $\text{ZnI}_2$  and  $\text{H}_2\text{O}$ , and yet were unable to detect  $\text{ZnI}_2$  with Raman spectroscopy.<sup>[10]</sup> Yang et al. found nanoparticle ligands and hydroxyl groups accelerated  $\text{MAPbX}_3$  degradation, but computationally predicted the deprotonation of  $\text{CH}_3\text{NH}_3^+$  by ZnO even in the absence of these surface groups.<sup>[20]</sup> Collectively, surface chemistry at the ZnO-perovskite interfaces has largely been assessed by monitoring the generation  $\text{PbI}_2$ .

Recent efforts have increased PCE for ZnO-based PSC to over 20% by addressing these stability concerns by “passivating” the surface with magnesium oxide, ethanolamine, polyethylenimine, and ZnS.<sup>[9,19,21–24]</sup> Despite these improvements however, the reactions of methylammonium cations at ZnO interfaces have remained unresolved, limiting the long-term stability of ZnO-perovskite solar cells. Additionally, these high efficiency devices have required ZnO annealing temperatures in excess of 500 °C, negating many of the potential advantages of ZnO.

In this work, we probe degradation mechanisms at the perovskite-ZnO interface by utilizing an amine indicator, investigating the generation of hydroxyl groups, and by monitoring the generation of ZnI<sub>2</sub>. We reveal the root cause of ZnO-perovskite instability to be the deprotonation of the methylammonium cation, leading to the formation of zinc hydroxide. Based on this finding, we replace the MA cation with lower acidity formamidinium mixed with cesium cations (FACs) in devices with low temperature (120 °C) processed ZnO. The FACs perovskite offers greatly enhances thermal stability, and we find in such a configuration that device stability compares favorably with SnO<sub>2</sub>, with ZnO offering superior UV stability to TiO<sub>2</sub>.

## Results and Discussion

Based on the previous studies,<sup>[20,21]</sup> and the nature of the amphoteric ZnO surface,<sup>[25,26]</sup> we hypothesize that the ZnO surface can abstract H<sup>+</sup> from an acid, which may then trigger the degradation process. In organic-inorganic metal halide perovskites, the organic cation (MA in MAPbI<sub>3</sub>) is the source of the H<sup>+</sup>. To elucidate the surface chemistry we design a series of experiments that probe the ZnO-perovskite interface. First, to determine whether ZnO can deprotonate the MA cation, we utilize an indicator molecule. Aromatic nitro compounds such as dinitrotoluene and dinitrobenzene are sensitive primary amine indicators.<sup>[27]</sup> 2,4-dinitrotoluene

(DNT) rapidly forms a Meisenheimer complex with methylamine, which has a characteristic blue-green colour due to an absorption minima between 450 and 500 nm. We add MAPbI<sub>3</sub> powder to nitrogen filled, sealed vials with and without bulk ZnO powder and then heat to 130 °C for 30 minutes. We then purge the headspace of these vials into a solution of dimethyl sulfoxide (DMSO) containing DNT. While gases from the vial with only MAPbI<sub>3</sub> result in a minimal absorption shift from the baseline solution of DMSO-DNT, gases sampled from the vial of MAPbI<sub>3</sub> with ZnO result in a visible blue-green color when introduced to the DMSO-DNT solution, a nearly dynamite confirmation that CH<sub>3</sub>NH<sub>2</sub> is indeed generated due to the deprotonation of MA as depicted in Figure 1 (a-c).

The abstraction of H<sup>+</sup> by the ZnO surface will give rise to Zn-O-H<sup>+</sup> which can undergo further changes to produce Zn-O-H. To confirm hydroxide formation is also part of the degradation mechanism, we utilize Fourier transform infrared spectroscopy (FTIR) to inspect ZnO-MAPbI<sub>3</sub> films during 100 °C annealing (Figure 1d). We use the acetonitrile solvent system for MAPbI<sub>3</sub>, as this provides high crystallinity films, as-cast at room temperature, allowing for initial inspection of the interface with minimal thermally induced effects.<sup>[28]</sup> We assign the peaks at 3138 and 3179 cm<sup>-1</sup> (Figure 1d) to symmetric and asymmetric stretching of NH<sub>3</sub><sup>+</sup>,<sup>[29]</sup> and the broad band around 3485 cm<sup>-1</sup> to O-H stretching from hydroxyl groups (or physically adsorbed water).<sup>[30–32]</sup> Additional annealing results in gradual accumulation of hydroxyl groups and the loss of CH<sub>3</sub>NH<sub>3</sub><sup>+</sup> to volatile CH<sub>3</sub>NH<sub>2</sub>. To exclude the possibility of lead hydrates being responsible for this spectral signature, we utilize x-ray photoelectron spectroscopy (XPS) to examine a ZnO film coated with only a thin layer (< 5 nm, non-continuous) of methylammonium iodide, and find the O 1s spectra clearly reveal the formation of a metal hydroxide (Figure S1). In addition to MA deprotonation, surface hydroxyl groups are an additional source of instability and have been previously shown to catalyse

MAPbI<sub>3</sub> decomposition.<sup>[10,20]</sup> The deprotonation of MA and hydroxylation of ZnO can also result in Zn-I bond formation, as a by-product of the degradation.

We utilize x-ray diffraction (XRD) under an inert atmosphere, since ZnI<sub>2</sub> is hygroscopic in nature. First, we add HI to bulk ZnO powder to produce ZnI<sub>2</sub>, and then spin-coat films and collect reference spectra (Figure S2). Next, we collect time dependent XRD of ZnO-MAPbI<sub>3</sub> films annealed at 100 °C. We observe an XRD peak emerge at 25.42° 2θ, which closely matches the American Society of Testing and Materials (ASTM) value of 25.45° for the (111) plane of tetragonal ZnI<sub>2</sub>,<sup>[33]</sup> and also matches the dominant peak of our highly oriented ZnI<sub>2</sub> reference spectra.

In the above investigations, we have revealed a mechanism for the intrinsic instability of ZnO with MAPbI<sub>3</sub> where the degradation is initiated by the proton abstraction causing the release of MA and formation of Zn-OH bonds (Figure 1f) and Zn-I bonds (Figure 1g).

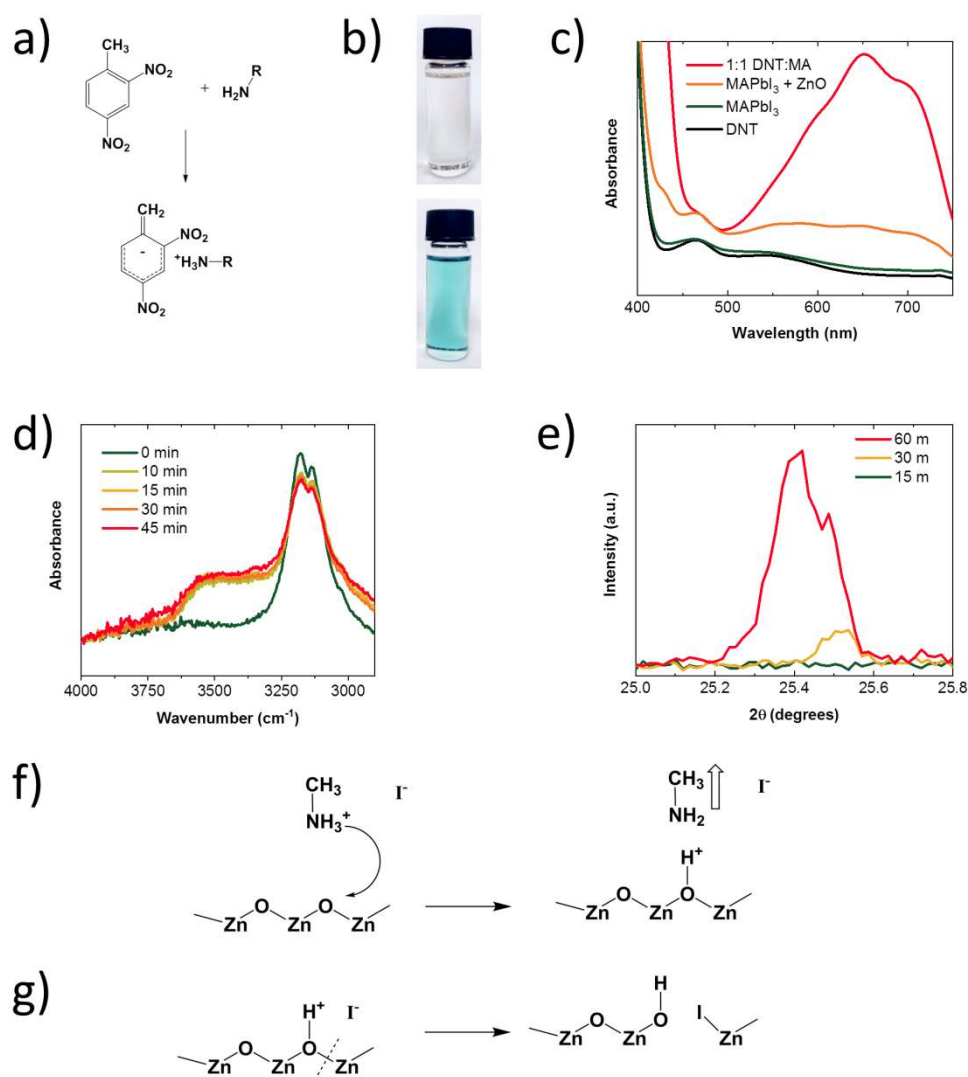


**Figure 1 | Probing the Degradation Mechanism of MAPbI<sub>3</sub>-ZnO.** **a)** Schematic of 2,4-dinitrotoluene (DNT) and a primary amine forming a Meisenheimer complex. **b)** DMSO solution containing 10 mM DNT without methylamine (top) and with 10 mM methylamine (bottom). **c)** Absorbance of solutions of DNT-DMSO before and after reacting with gases collected from MAPbI<sub>3</sub> and ZnO. **d)** FTIR spectra of MAPbI<sub>3</sub> film annealed on ZnO as a function of time. **e)** XRD of ZnI<sub>2</sub> (111) peak intensity increasing with annealing time for ZnO-MAPbI<sub>3</sub> films. **f)** Schematic for ZnO abstracting H<sup>+</sup> from CH<sub>3</sub>NH<sub>3</sub><sup>+</sup>, forming Zn-O-H<sup>+</sup>; CH<sub>3</sub>NH<sub>2</sub> evaporates. **g)** Schematic for formation of Zn-I bonds.

After confirming the perovskite-ZnO instability resulting from the MA cation, we speculate that decreasing the acidity of the A site cation should improve the thermal stability of the interface

(pKa of MA is  $\sim 10.6$ ). To that end, we introduce the less acidic formamidinium (FA) cation, with a pKa of 11.5, in the mixed FA and Cs cation system as a replacement for MA.<sup>[9,34]</sup> “In the case of the FA cation, the positive charge is resonance stabilised due to the presence of two ‘N’ centres and thus has lower acidity than the MA cation, which is not resonance stabilized. We note that while ZnO could abstract a proton from the FA cation, the rate of the reaction is expected to be considerably slower compared to the MA cation owing to the lower acidity of FA. We confirm this expectation utilizing the amine detector developed previously (Figure 1a-c). While the perovskite with MA cations produces sufficient amines for detection after annealing at 130 °C for 30 minutes, the perovskite with FA and Cs cations does not produce an appreciable absorbance change in the indicator solution, even after doubling the annealing time. After increasing the annealing temperature to 200 °C we finally observe a small change in absorbance of the indicator solution (Figure S3), which demonstrates the versatility of dinitrotoluene in detecting the degradation of these organic cations.”

To examine the stability of perovskite thin films we prepare  $\text{FA}_{0.83}\text{Cs}_{0.17}\text{Pb}(\text{I}_{0.83}\text{Br}_{0.17})_3$  (from now on termed FACs) on ZnO coated FTO and anneal at 100 °C from 5 to 60 minutes before collecting X-ray diffraction scans. For completeness, we also compare stability to the  $\text{Cs}_{0.05}(\text{FA}_{0.83}\text{MA}_{0.17})_{0.95}\text{Pb}(\text{I}_{0.83}\text{Br}_{0.17})_3$  perovskite (from here on termed CsFAMA), which is one of the highest performing contemporary perovskite compositions and has also been used frequently in recent ZnO studies.<sup>[18,21,24]</sup> While there is an initial increase in crystallinity for  $\text{MAPbI}_3$  from 5 to 15 minutes, continued annealing past this time results in the rapid generation of  $\text{PbI}_2$ , shown by a dominant XRD peak and a yellowed film (Figure 2a). Thermal stability of the CsFAMA perovskite is improved, but the  $\text{PbI}_2$  peak intensity is greater than the (110) perovskite reflection after an hour of annealing (Figure 2b). Close inspection of the CsFAMA film also reveals voids and cracks forming at the ZnO interface (we show high resolution grayscale SEM images in Figure S4). In contrast,



after one hour of annealing of the FACs perovskite at 100 °C the film remains dark and uniform, while a small  $\text{PbI}_2$  peak is seen in the XRD scan (Figure 2c). Remarkably, while the  $\text{PbI}_2$  peak intensity increases substantially for the  $\text{ZnO-MAPbI}_3$  films from 30 to 60 minutes of annealing, the peak intensity remains virtually unchanged over this period for the FACs-ZnO films, indicating greatly reduced thermal degradation. We also observe a similar trend on  $\text{SnO}_2$ , with CsFAMA perovskite being less thermally stable than FACs, which highlights the importance of using methylammonium-free perovskites for long-term stability in devices employing metal oxide charge transport layers (Figure S5).

In order to assess stability in operating conditions, we fabricate devices with MA, CsFAMA, and FACs perovskite layers on ZnO and leave under  $\sim 1$  sun illumination ( $76 \text{ mWcm}^{-2}$  Xenon lamp solar aging box) at 60 °C for 8 hours. We cross-section the devices to inspect the interface with SEM and find dramatic differences depending on the choice of cation. Devices containing MA have numerous voids at a visually degraded perovskite-ZnO interface, devices with CsFAMA show the emergence of smaller voids at the interface, and the devices with FACs cations retain conformal contact between the perovskite and ZnO (Figure 2 d-f). The presence of voids in the perovskite, originating at the ZnO interface, is explainable by the generation of methylamine gas when the MA cation is deprotonated. Methylamine gas has previously been shown to “melt”  $\text{MAPbI}_3$  upon exposure.<sup>[35]</sup> We postulate that the combination of loss of material (methylammonium halide), along with local melting of the perovskite in close proximity to the degradation sites, is responsible for the void growth.

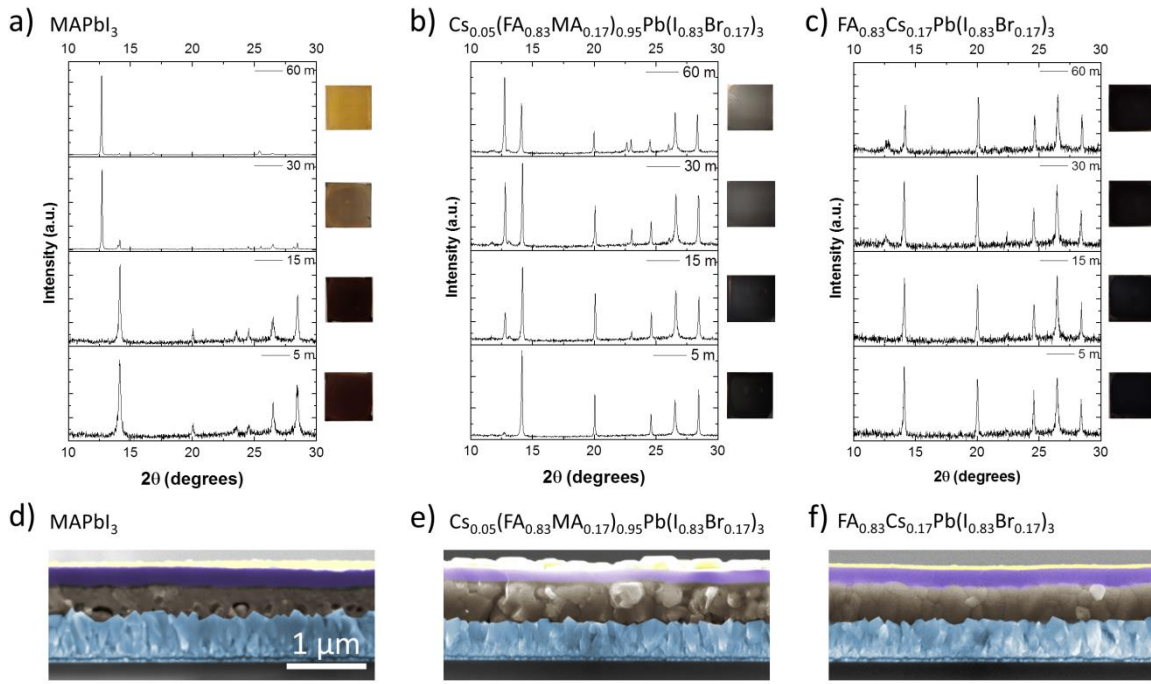


**Figure 2 | Thermal Stability of Perovskites on Zinc Oxide.** **a)** MAPbI<sub>3</sub> rapidly decomposes as 100°C annealing proceeds past 30 minutes, as indicated by a dominant PbI<sub>2</sub> peak and yellow film. The PbI<sub>2</sub> peak intensity increases sharply at 60 minutes of annealing, as the film is converted almost entirely to PbI<sub>2</sub>. **b)** CsFAMA film offers greater stability but still displays clear discoloration after an hour of annealing. **c)** FACs perovskite shows a small PbI<sub>2</sub> peak after 30 minutes of annealing, and the peak intensity remains unchanged after additional annealing time. **d)** False-color SEM cross-section of MAPbI<sub>3</sub> devices with ZnO after aging 8 hours of unencapsulated aging (1 sun illumination, 60 °C, ~50% humidity). **e)** SEM cross-section of aged CsFAMA device. **f)** SEM cross-section of aged FACs device.

Next, we compare the stability of FACs PSC under UV irradiation and thermal stressing for devices containing ZnO, TiO<sub>2</sub>, and SnO<sub>2</sub> electron transport layers (ETL). First, we examine device degradation under a high intensity UV lamp and find that devices containing TiO<sub>2</sub> rapidly degrade, losing half of their power conversion efficiency in just 10 minutes and all power output within one hour (Figure 3a). One explanation for this instability is that upon photo-excitation of TiO<sub>2</sub>, holes in the valence band recombine with electrons at oxygen adsorption sites, desorbing oxygen and

creating deep trap states.<sup>[6]</sup> Surprisingly, while SnO<sub>2</sub>-based PSC have recently shown improved stability over TiO<sub>2</sub> for long term stability in ambient operating conditions,<sup>[7]</sup> we find ZnO exhibits the best UV stability of the three metal oxides. ZnO is known to be UV sensitive as a material, but our results suggest that unlike TiO<sub>2</sub>, deep electron traps are not generated in the ZnO upon UV exposure. Adding a thin layer of C<sub>60</sub> to isolate the perovskite from direct ZnO contact further improved UV stability of the ZnO-perovskite interface (Figure 3a), similar to previous observations with SnO<sub>2</sub> and TiO<sub>2</sub> charge extraction layers.<sup>[35,36]</sup> Next, we probed the thermal stability by holding devices at 85 °C in ambient atmosphere and periodically testing their performance (Figure 3b). Devices with ZnO and MA cations show markedly reduced stability relative to those with FACs cations. While the C<sub>60</sub> passivation layer increased ZnO device longevity under UV irradiation, the reduced thermal stability with C<sub>60</sub> indicates different origins for thermally and UV induced degradation. Early in the thermal stability test, the C<sub>60</sub> passivated ZnO provides better photovoltaic performance than unpassivated ZnO. However, as aging continues we observe reduced V<sub>oc</sub> and lower fill factor (which we show in Figure S6) relative to the unpassivated ZnO. The origin of the lower thermal stability with C<sub>60</sub> is not clear, especially since we have previously observed that the addition of C<sub>60</sub> to n-i-p cells employing a SnO<sub>2</sub> n-layer has improved the stability under combined light and heat (albeit at lower temperatures to our present study). A possible explanation is that C<sub>60</sub> is known to aggregate and crystallize under thermal stress. It may be that the smooth crystalline ZnO surface presents a specifically “slippery” surface for C<sub>60</sub> molecules. Previous observations of fullerenes under thermal stress have revealed that aggregations grow to the micron-scale, which would form shunt paths responsible for our observed fill factor and voltage losses (shown in Figure S6).<sup>[37]</sup>

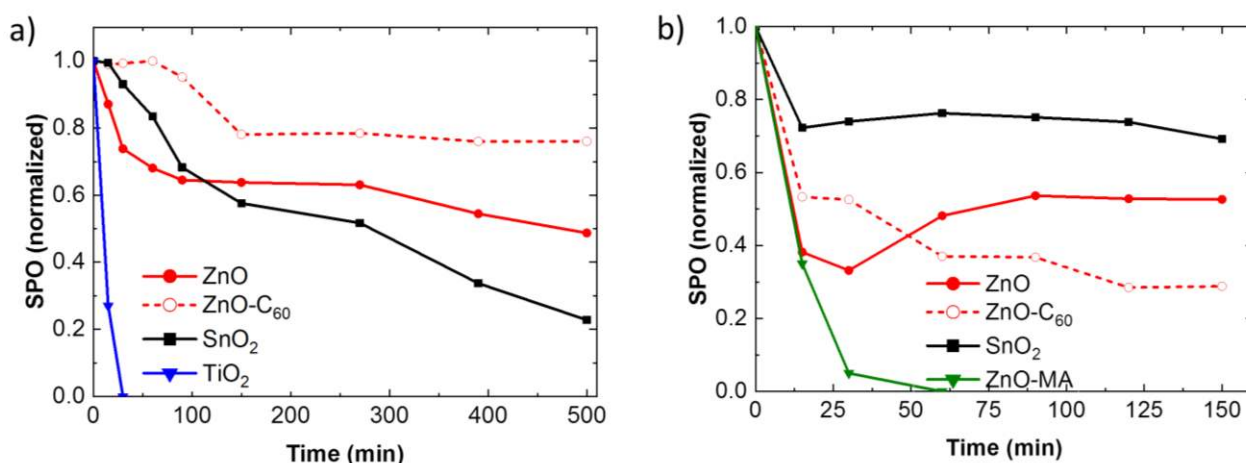


**Figure 3 | UV and Thermal Stability of FACs PSC on Metal Oxides** **a)** Under high intensity UV (365nm LED, equivalent to 12 suns UV component of AM 1.5 spectrum). **b)** Thermal stability of devices aged at 85 °C in air. All devices in UV and thermal stability tests utilized the FA<sub>0.83</sub>CS<sub>0.17</sub>Pb(I<sub>0.83</sub>Br<sub>0.17</sub>)<sub>3</sub> perovskite except for ZnO-MA, which utilized MAPbI<sub>3</sub>.

Having improved stability of the ZnO-perovskite interface by eliminating the MA cation, we now investigate the device performance. Scanned efficiency of devices based on SnO<sub>2</sub> and ZnO achieved efficiencies of 20.3 and 21.1%, with 19.7% and 18.0% steady-state power output (SPO), respectively. We show additional photovoltaic parameters in Figures S7 and S8. Scanned efficiency gains for ZnO devices over SnO<sub>2</sub> analogues are primarily driven by increased open-circuit voltage and a slight increase in fill factor, while median current density decreased slightly due to the greater parasitic absorption of ZnO in UV region of the spectrum (Figure S9). We note the optical transmittance of ZnO can be increased with a variety of dopants, and B and F doping was recently shown to improve transmittance to 99.8% from 92.8% for undoped ZnO, but we evaluate only undoped ZnO for this study.<sup>[11,38]</sup> The lower steady-state power output of the ZnO-containing cells, can be attributed in part to increased hysteresis relative to SnO<sub>2</sub> based cells. This is likely to originate due to an increased surface recombination velocity.<sup>[39]</sup> This may be due to either macroscopic defects on one of the charge extraction layers, enabling contact of the electrodes to

the perovskite absorber layer, or a higher density of surface traps at the ZnO perovskite interface, responsible for trap assisted recombination. The activity of the surface recombination sites can be modulated by migration of ions.<sup>[39,40]</sup> We also note that we have observed large aggregates in the ZnO films, which we show in the atomic force microscope images in Figure S10. It may be that these “spikes” in the ZnO are responsible for shorting paths in the solar cells, or induce pinholes in the perovskite films or subsequent layers, which may also contribute to the lower than anticipated SPO. Recent work has shown a thin passivating layer of MgO and ethanolamine, or ZnS, effectively eliminates hysteresis in ZnO-based PSC.<sup>[21,24]</sup>

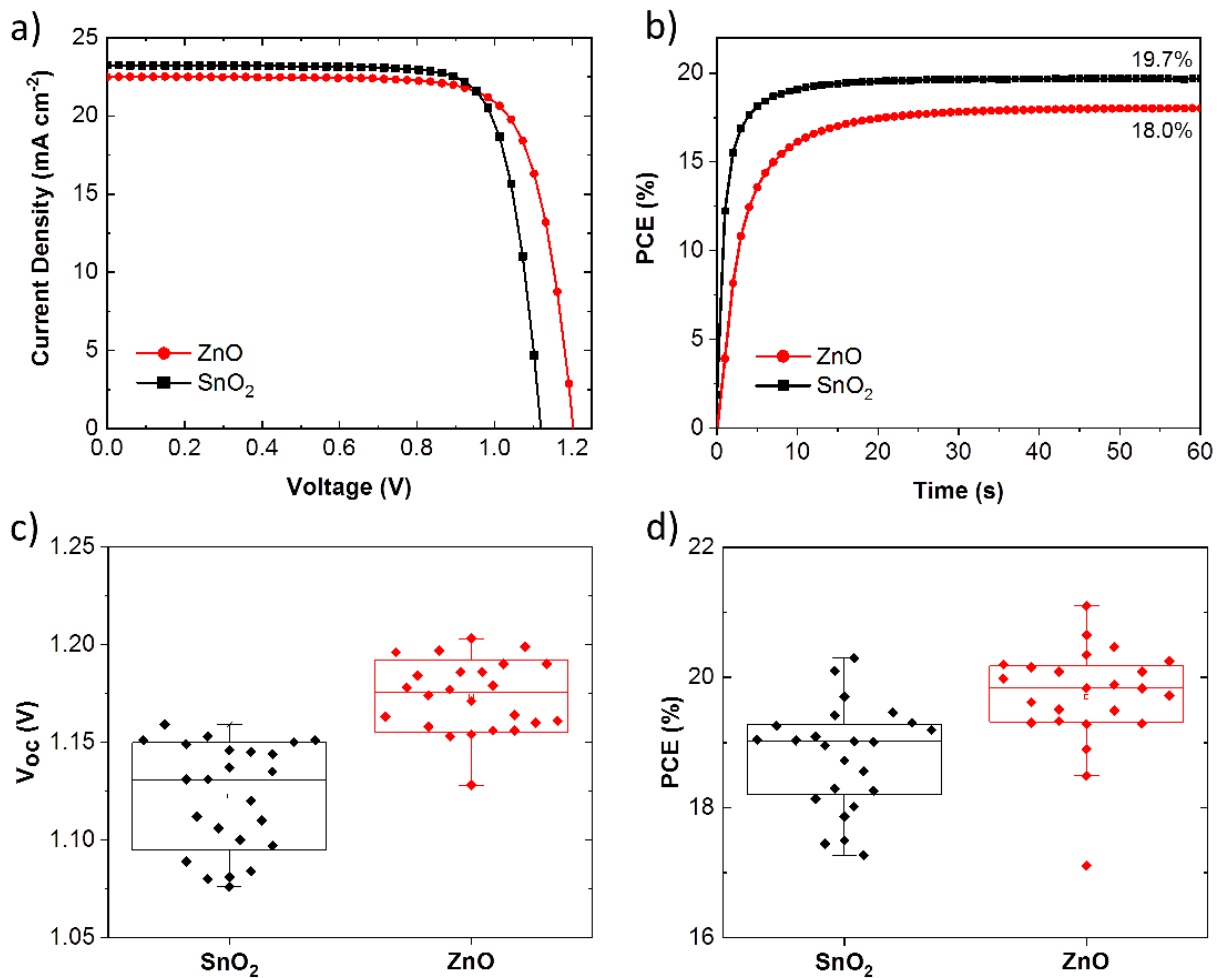


**Figure 4 | Photovoltaic Performance of Formamidinium-Cesium Perovskite Solar Cells Utilizing ZnO and SnO<sub>2</sub> Electron Transport Layers. a) Champion SnO<sub>2</sub> and ZnO-based devices. b) Steady**

state power output of devices comprising  $\text{SnO}_2$  and ZnO. **c)** PCE improvements on ZnO devices are driven primarily by improved open circuit voltage. **d)** PCE for 24 devices.

To better understand the origin of the ZnO-based device performance, we utilize Kelvin probe and spectroscopic techniques to assess the quality of metal oxide-perovskite interfaces. Often, surface photo voltage (SPV) spectroscopy is used to probe the change in surface band bending under illumination. Here, we investigate the complete device stack, including the electron extraction layer, perovskite absorber layer, and hole transport layer. We expect the surface photovoltage of the complete device stack to reflect the open-circuit voltage generated within the cell.<sup>[41]</sup> Because ZnO-based PSC show greater hysteresis than those with  $\text{SnO}_2$  (Figure S11), we first confirm the voltage increases of the ZnO-based PSC were not an artefact of scanning. We use Kelvin probe based surface photo-voltage (SPV) measurement to assess the interface behavior, and see ~120 mV higher SPV for the ZnO/perovskite/Spiro-OMeTAD stack compared to their  $\text{SnO}_2$  counterpart (Figure 5a), confirming a meaningful open-circuit voltage improvement. We also observe similar behavior for the stacks without the Spiro-OMeTAD layer (as shown in Figure S12), indicating that the voltage improvement for ZnO-based devices is mostly due to the difference in the metal oxide-perovskite interfaces. Next, to determine whether the increased voltage results from decreased non-radiative recombination at the ZnO interface we utilize photoluminescence spectroscopy. We observe more than 7 fold higher steady state photoluminescence (PL) intensity from perovskite films on ZnO, in comparison to perovskite films on  $\text{SnO}_2$ , and time-resolved PL (TRPL) reveals average carrier lifetimes also improve from 65.7 ns to 134.4 ns (Figure 5b,c). We note that treating ZnO with UV Ozone for 15 minutes substantially enhances the PL intensity, which may be due to removing organic contamination from the surface and/or removing defect sites in the ZnO by filling oxygen vacancies.<sup>[42,43]</sup> There is also a slight shift in photoluminescence maxima for perovskite films on ZnO and  $\text{SnO}_2$  (767 and 765 nm, respectively), which may be due to slight

changes in crystallization or stoichiometry of perovskite films on these metal oxides which has been previously observed with TCO's.<sup>[18]</sup> The metal oxides also have different refractive indices, and this very small shift in emission wavelength may be due to an optical effect. We also measure photoluminescence quantum efficiency (PLQE) of perovskite films on SnO<sub>2</sub> and ZnO to more directly assess the interface defects. When excited with a 405 nm laser absorbed near the metal oxide interface, PLQE of perovskite on ZnO increases substantially relative to the SnO<sub>2</sub> counterpart (Figure 5d), with values of 1.07% and 0.05% respectively, under  $\sim 100 \text{ mWcm}^{-2}$  irradiance. The increase in steady state PL emission, longer carrier lifetime, and improved PLQE are consistent with ZnO having reduced non-radiative recombination at the metal oxide-perovskite interface relative to SnO<sub>2</sub>, which is consistent with the increased  $V_{oc}$ .<sup>[44,45]</sup>

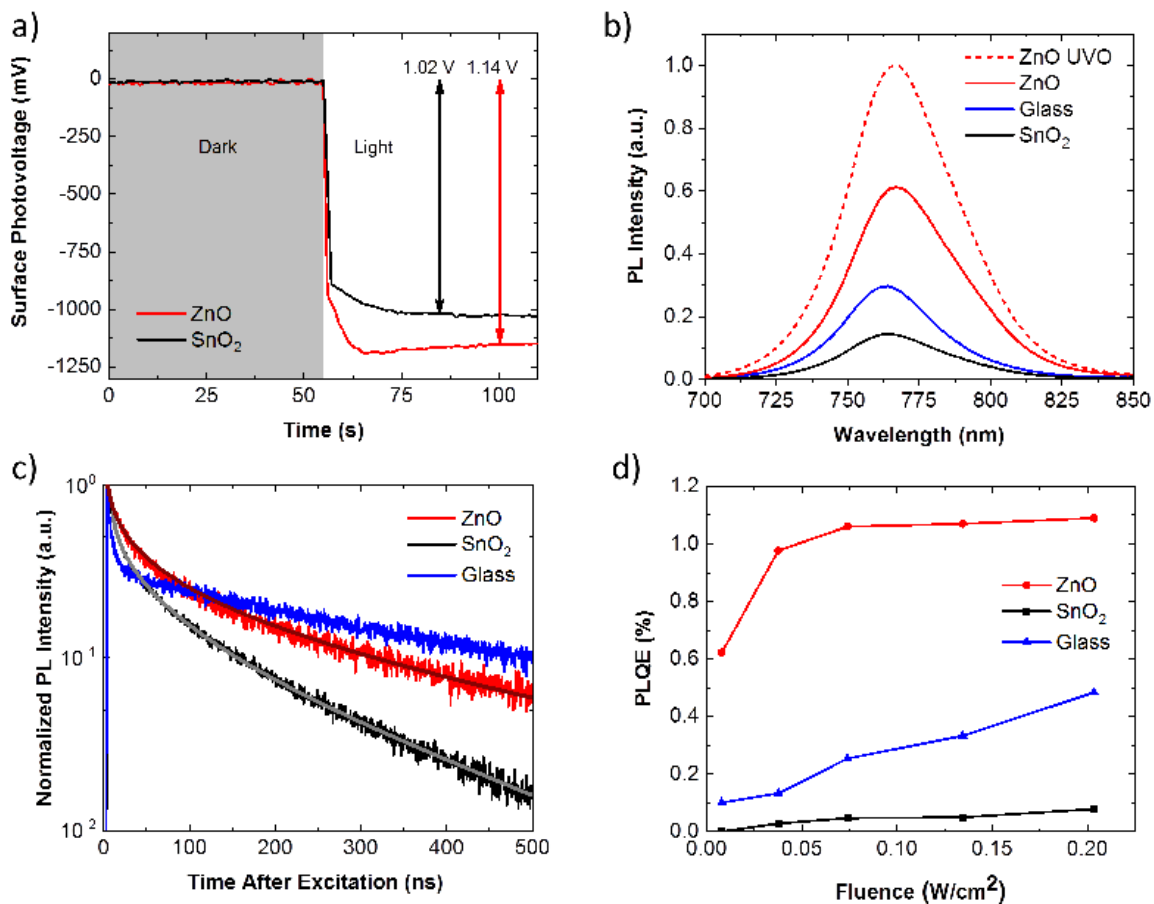


**Figure 5 | ZnO and SnO<sub>2</sub> Interfacial Data.** **a)** Kelvin probe measurement of surface photo-voltage of ZnO and SnO<sub>2</sub>/perovskite/Spiro-OMeTAD films on FTO substrates. **b)** Steady state

photoluminescence of FACs perovskite on SnO<sub>2</sub> and ZnO coated FTO. **c)** Time resolved photoluminescence spectroscopy of FACs perovskite on SnO<sub>2</sub> and ZnO substrates on FTO. **d)** PLQE of perovskite films on ZnO and SnO<sub>2</sub> coated FTO and quartz glass.

## Conclusion

Here, we have assessed the mechanism driving the instability of metal halide perovskite solar cells processed on ZnO n-type charge extraction layers. Collectively, through amine detection, FTIR evidence of zinc hydroxyl groups, XRD confirmation of ZnI<sub>2</sub>, and cross-sectional SEM images, we elucidate the precise reactions occurring at the ZnO-MAPbI<sub>3</sub> interface which decompose the perovskite. We demonstrate that PSCs employing ZnO offer competitive efficiency and stability to other leading metal oxides, once the MA cation is replaced with formamidinium and cesium. These results encourage renewed interest in ZnO for high performance perovskite solar cells, especially for low temperature processed devices on flexible substrates, and to help compatibilize perovskite solar cells with aluminium doped zinc oxide transparent conducting oxide electrodes.

## Acknowledgements

We thank the EPSRC, UK for support. KS thanks the Marshall Aid Commemoration Commission. B.W. acknowledges funding from the European Commission via a Marie-Skłodowska-Curie individual fellowship (REA Grant Number 706552-APPEL). The research leading to these results has received funding from the European Union's Horizon 2020 research and innovation programme under grant agreement No. 763977 of the PerTPV project.

## References

- [1] C. K. Hong, *Nanoscale* **2016**, *8*, 10528.



- [2] N. Park, *Biochem. Pharmacol.* **2015**, *18*, 65.
- [3] W. Chen, Y. Wu, J. Liu, C. Qin, X. Yang, *Energy Environ. Sci.* **2015**, 629.
- [4] P. Liang, C. Chueh, S. T. Williams, A. K. Jen, *Adv. Energy Mater.* **2015**, 1.
- [5] NREL Efficiency Chart. <https://www.nrel.gov/pv/assets/pdfs/pv-efficiency-chart.20181221.pdf> **2018**.
- [6] T. Leijtens, G. E. Eperon, S. Pathak, A. Abate, M. M. Lee, H. J. Snaith, *Nat. Commun.* **2013**, *4*, 1.
- [7] J. A. Christians, P. Schulz, J. S. Tinkham, T. H. Schloemer, S. P. Harvey, B. J. T. De Villers, A. Sellinger, J. J. Berry, J. M. Luther, *Nat. Energy* **2018**, *3*, 68.
- [8] K. Choi, J. Lee, H. Il Kim, C. W. Park, G. Kim, H. Choi, S. Park, S. A. Park, T. Park, *Energy Environ. Sci.* **2018**, 17.
- [9] X. Zhao, H. Shen, Y. Zhang, X. Li, X. Zhao, M. Tai, J. Li, J. Li, X. Li, H. Lin, *ACS Appl. Mater. Interfaces* **2016**.
- [10] Y. Dkhissi, S. Meyer, D. Chen, H. C. Weerasinghe, L. Spiccia, Y. Cheng, R. A. Caruso, *ChemSusChem* **2016**, 687.
- [11] S. C. Dixon, D. O. Scanlon, J. Carmalt, I. P. Parkin, *J. Mater. Chem. C* **2016**.
- [12] B. Q. Zhang, C. S. Dandeneau, X. Zhou, G. Cao, *Adv. Mater.* **2009**, 4087.
- [13] A. Miglio, D. Waroquiers, G. Rignanese, X. Gonze, *Chem. Mater.* **2014**, *26*, 5447.
- [14] K. Mahmood, M. Taqi, *RSC Adv.* **2017**, *7*, 17044.
- [15] Y. Lin, S. R. Thomas, H. Faber, R. Li, M. A. Mclachlan, P. A. Patsalas, T. D. Anthopoulos, *Adv.*

- [16] S. Bai, Z. Wu, X. Wu, Y. Jin, N. Zhao, Z. Chen, Q. Mei, *Nano Res.* **2014**, *7*, 1749.
- [17] CHEOPS Project, Life-Cycle Assessment of Silicon-Perovskite Tandem Solar Cells  
<https://www.cheops-project.eu/news-in-brief/first-results-regarding-the-environmental-impact-of-perovskitesilicon-tandem-pv-modules> **2018**.
- [18] B. Dou, E. M. Miller, A. Christians, E. M. Sanehira, T. R. Klein, F. S. Barnes, S. E. Shaheen, S. M. Garner, S. Ghosh, A. Mallick, D. Basak, M. F. A. M. Van Hest, **2017**.
- [19] Y. Cheng, Q. Yang, J. Xiao, Q. Xue, H. Li, Z. Guan, H. Yip, S. Tsang, *ACS Appl. Mater. Interfaces* **2015**, *7*, 19986.
- [20] J. Yang, B. D. Siempelkamp, E. Mosconi, F. De Angelis, T. L. Kelly, *Chem. Mater.* **2015**, *27*, 4229.
- [21] J. Cao, B. Wu, R. Chen, Y. Wu, Y. Hui, B. Mao, *Adv. Mater.* **2018**, *1705596*, 1.
- [22] K. Mahmood, M. T. Mehran, F. Rehman, M. S. Zafar, S. W. Ahmad, R. Song, *ACS Omega* **2018**, *3*, 9648.
- [23] F. Qin, W. Meng, J. Fan, C. Ge, B. Luo, R. Ge, L. Hu, F. Jiang, T. Liu, Y. Jiang, Y. Zhou, *ACS Appl. Mater. Interfaces* **2017**, *9*, 26045.
- [24] R. Chen, J. Cao, Y. Duan, Y. Hui, T. T. Chuong, D. Ou, F. Han, F. Cheng, X. Huang, B. Wu, N. Zheng, *J. Am. Chem. Soc.* **2018**, jacs. 8b11001.
- [25] A. Janotti, C. G. Van De Walle, *Reports Prog. Phys.* **2009**.
- [26] A. Degen, M. Kosec, *J. Eur. Ceram. Soc.* **2000**, *20*, 667.
- [27] A. L. Hunt, S. C. K. Yong, J. F. Alder, M. Iqd, *Anal. Commun.* **1996**, *33*, 323.

- [28] N. K. Noel, S. N. Habisreutinger, B. Wenger, M. T. Klug, M. T. Hörantner, M. B. Johnston, R. J. Nicholas, D. T. Moore, H. Snaith, *Energy Environ. Sci.* **2016**.
- [29] T. Glaser, C. Müller, M. Sendner, C. Krekeler, O. E. Semonin, T. D. Hull, O. Yaffe, J. S. Owen, W. Kowalsky, A. Pucci, R. Lovrinčić, *J. Phys. Chem. Lett.* **2015**, 6, 2913.
- [30] Van De Walle CG, *Phys. Rev. Lett.* **2000**, 85, 1012.
- [31] A. Top, H. Çetinkaya, *Mater. Chem. Phys.* **2015**, 167, 77.
- [32] M. Y. Ghotbi, *J. Alloys Compd.* **2010**, 491, 420.
- [33] I. A. Kariper, *Opt. Mater. (Amst).* **2015**, 44, 78.
- [34] T. J. Groshens, R. A. Hollins, *Chem. Commun.* **2009**, 3089.
- [35] Z. Wang, D. P. McMeekin, N. Sakai, S. van Reenen, K. Wojciechowski, J. B. Patel, M. B. Johnston, H. J. Snaith, *Adv. Mater.* **2017**, 29.
- [36] K. Wojciechowski, T. Leijtens, S. Siprova, C. Schlueter, M. T. Hörantner, J. T. W. Wang, C. Z. Li, A. K. Y. Jen, T. L. Lee, H. J. Snaith, *J. Phys. Chem. Lett.* **2015**, 6, 2399.
- [37] M. Campoy-quiles, T. Ferenczi, T. Agostinelli, P. G. Etchegoin, Y. Kim, T. D. Anthopoulos, P. N. Stavrinou, D. D. C. Bradley, J. Nelson, *Nat. Mater* **2008**, 7, 158.
- [38] K. Mahmood, M. Taqi, *RSC Adv.* **2017**, 7, 17044.
- [39] S. Van Reenen, M. Kemerink, H. J. Snaith, *J. Phys. Chem. Lett.* **2015**, 6, 3808.
- [40] P. Calado, A. M. Telford, D. Bryant, X. Li, J. Nelson, B. C. O. Regan, P. R. F. Barnes, *Nat. Commun.* **2016**, 7, 13831.
- [41] F. Lenzmann, J. Krueger, S. Burnside, K. Brooks, M. Gra, D. Gal, S. Ru, D. Cahen, *J. Phys.*

*Chem. B* **2001**, 6347.

- [42] G. Gonc, *J. Non. Cryst. Solids* **2006**, 352, 1444.
- [43] C. E. Small, S. Chen, J. Subbiah, C. M. Amb, S. W. Tsang, T. H. Lai, J. R. Reynolds, F. So, *Nat. Photonics* **2012**, 6, 115.
- [44] M. Stolterfoht, C. M. Wolff, J. A. Márquez, S. Zhang, C. J. Hages, D. Rothhardt, S. Albrecht, P. L. Burn, P. Meredith, T. Unold, D. Neher, *Nat. Energy* **2018**, 3, 847.
- [45] J. P. Correa-Baena, W. Tress, K. Domanski, E. H. Anaraki, S. H. Turren-Cruz, B. Roose, P. P. Boix, M. Grätzel, M. Saliba, A. Abate, A. Hagfeldt, *Energy Environ. Sci.* **2017**, 10, 1207.